Achieving Large and Anisotropic Spin-mediated Thermal Transport in Textured Quantum Magnets

Shucheng Guo,[1] Xue Bai,[2] Boqun Liang,[3] Thomas Hoke,[1] Ming Liu,[1,3] Rafal E. Dunin-Borkowski,[2] Xi Chen[1,3,*]

1. Department of Electrical and Computer Engineering, University of California, Riverside, California, 92521, USA

2. Ernst Ruska-Centre for Microscopy and Spectroscopy with Electrons, Forschungszentrum Jülich, Jülich, 52425, Germany

3. Materials Science and Engineering program, University of California, Riverside, California, 92521, USA

*Correspondence: xichen@ucr.edu

Keywords

spin-mediated thermal conductivity, anisotropic thermal properties, textured quantum magnets, solvent-cast cold pressing

Abstract

Spin excitations, including magnons and spinons, can carry thermal energy and spin information. Studying spin-mediated thermal transport is crucial for spin caloritronics, enabling efficient heat dissipation in microelectronics and advanced thermoelectric applications. However, designing quantum materials with controllable spin transport is challenging. Here, we synthesize highly textured spin-chain compound Ca_2CuO_3 using a solvent-cast cold pressing technique, aligning two-dimensional nanostructures with spin chains perpendicular to the pressing direction. The sample exhibits high thermal conductivity anisotropy and an excellent room-temperature thermal conductivity of 12 ± 0.7 W m^{-1} K^{-1}, surpassing all polycrystalline quantum magnets. Such a high value is attributed to the significant spin-mediated thermal conductivity of 10 ± 1 W m^{-1} K^{-1}, the highest reported among all polycrystalline quantum materials. Analysis through a one-dimensional kinetic model suggests that near room-temperature, spinon thermal transport is dominated by coupling with high-frequency phonons, while extrinsic spinon-defect scattering is negligible. Additionally, this method was used to prepare textured La_2CuO_4, exhibiting highly anisotropic magnon thermal transport and demonstrating its broad applicability. A distinct role of defect

scattering in spin-mediated thermal transport is observed in two spin systems. Our findings open new avenues for designing quantum materials with controlled spin transport for thermal management and energy conversion.

1. Introduction

Spin excitations, including spinons and magnons, are collective excitations in quantum magnets. Spinons can be observed in one-dimensional (1D) antiferromagnetic Heisenberg spin chains and other spin systems, functioning as quasiparticles with a spin of 1/2.[1] Magnons are commonly found in quasi-1D spin-ladders, two-dimensional (2D) spin-planes, and three-dimensional (3D) spin structures, typically exhibiting the behavior of spin-1 bosons.[2] These spin excitations carry both thermal energy and spin angular momentum through their collective motions.[3–6] Studying spin-mediated thermal transport is crucial for spin caloritronics,[7] as it can facilitate the spin Seebeck effect by enabling spin currents generated by a temperature (T) gradient.[8] Moreover, spin excitations can provide insights into the spin states of electrons in materials, making them promising candidates for applications in quantum information processing.[9,10]

In ideal 1D spin-chain systems that follow the conservation law of energy current,[11,12] spin excitations are gapless,[13] and intrinsic spinon-spinon coupling contributes no resistance.[14,15] The strong exchange interaction (J/k_B, where k_B denotes the Boltzmann constant) within the chains enables spinons to propagate at high group velocities,[13,16,17] thereby promoting ballistic spinon thermal transport and leading to infinite thermal conductivity along the chains at non-zero temperatures.[18] However, in real case, the extrinsic factors such as defects,[19–22] grain boundaries,[23,24] and interactions with other quasiparticles like phonons[19,25,26] and charge carriers[27] can affect spinon transport, leading to a finite spinon mean free path (l_s). As a result, large values of spinon thermal conductivity (κ_s) following the chain direction have been reported in several spin-chain materials, including Sr_2CuO_3, $SrCuO_2$, and Ca_2CuO_3,[5,18,28,29] making them promising candidates for thermal management applications, such as efficient heat dissipation and thermal interface materials.[30,31] Optimizing the alignment of spin chains can significantly reduce thermal resistance in the desired direction, thereby preventing devices from overheating, extending lifespan, and enhancing energy efficiency.[32] Most previous studies on thermal management materials have primarily focused on controlling phonon transport.[33,34] In contrast, spin excitation transport is

usually sensitive to external magnetic fields,[35,36] making spin-chain compounds ideal for dynamic thermal management in high-performance electronic devices.

To enable practical applications, it is essential to synthesize quantum magnets with enhanced, controllable spin-mediated thermal conductivity and pronounced anisotropic properties. Although single crystals can be grown along the spin-chain direction, they face significant drawbacks for industrial use. Their poor mechanical properties and limited scalability—typically confined to millimeter-scale sizes—restrict their suitability for large-scale applications. Furthermore, crystal growth requires significant energy consumption, extended preparation time, and stringent growth conditions.[37] For example, growing a Ca_2CuO_3 single-crystal using the travel solvent floating zone method requires maintaining T above 900 ˚C for over 3 days, along with substantial oxygen consumption.[28] In contrast, preparing large, textured polycrystals offers a more practical pathway. However, current preparation methods have notable limitations. For instance, textured spin ladder compounds have been obtained by repeating pressing processes.[23] Yet, the typically granular morphology of the grains and their random growth orientations create significant challenges in achieving highly textured samples, leading to a limited enhancement of κ.[23] Laser scanning has also been used to achieve anisotropic spin-chain patterning for microscale heat flow control. However, it struggles to maintain anisotropic growth at higher scanning speeds and requires experimental verification of κ of the obtained sample.[38] Thus, there is a strong need to develop novel methods to prepare highly textured magnetic materials with large κ_s.

Previous studies of spinon thermal transport have focused on single crystals. It has been found that a large l_s is close to the average distance between defects at low T, suggesting ballistic spinon thermal transport in $SrCuO_2$ and Sr_2CuO_3.[19,39] In addition, research into extrinsic effects on magnetic heat transport in Ca_2CuO_3 has provided experimental evidence of weak spinon-phonon coupling in these 1D spin-chain compounds.[28] However, there is limited research on thermal transport in polycrystalline quantum magnets, particularly in 1D spin-chain systems. A deeper understanding of the impacts of defects and grain boundaries on spin scattering processes is crucial for advancing our knowledge of spin-mediated thermal transport at the nanoscale.

In this work, we realized large and anisotropic spinon thermal transport in the highly textured spin-chain compound Ca_2CuO_3, fabricated by consolidating Ca_2CuO_3 nano-leaves through a solvent-cast cold pressing (SCCP) technique that we developed. As confirmed by scanning electron

microscopy (SEM), X-ray diffraction (XRD) and Raman spectroscopy studies, the grains are preferentially aligned with the spin chains perpendicular to the pressing direction. Thereby, we achieved a high room-temperature κ of 12 ± 0.7 W m^{-1} K^{-1}, exceeding that of all polycrystalline quantum magnets. This large κ is mainly due to the significant spin-mediated contribution of nearly 10 ± 1 W m^{-1} K^{-1}, which is the largest among all reported polycrystalline quantum materials. Furthermore, the aspect ratio of κ reached 4.5, nearing the maximum value observed in single-phase polycrystalline materials. Compared to a sample made using the conventional cold-pressing (CP) method, κ_s of the textured sample increased by approximately 50%. In addition, the spinon transport and scattering processes were studied using a kinetic model for 1D spinon transport. Moreover, the SCCP method was applied to prepare textured La_2CuO_4 with large anisotropic magnon thermal transport, where the aspect ratio of magnon thermal conductivity (κ_m) reaches about 5, underscoring its wide-ranging potential. Furthermore, we compared the thermal transport mechanisms of spin excitations across different quantum magnets, revealing the distinct roles of defect scattering. Our findings, which provide useful insights into understanding and enhancing spin-mediated thermal transport in magnetic polycrystals, are beneficial for developing novel devices for thermal management and energy conversion.

2. Results and Discussion

2.1 Crystallographic Information and Structural Characterization

As depicted in Figures 1A and B, Ca_2CuO_3 belongs to the orthorhombic crystal system[40] and behaves as a 1D spin-1/2 Heisenberg antiferromagnet, with spin chains formed by 180° Cu-O-Cu bonds along the b-axis.[13,16] In the ground state, it exhibits strong antiferromagnetic coupling between adjacent antiparallel spins,[41,42] characterized by a strong J/k_B of approximately 2000 K,[16] while the interchain interaction is much weaker, leading to highly anisotropic magnetic behavior.[13]

2D nano-leaves of Ca_2CuO_3 were prepared using a hydrothermal treatment followed by calcination, as shown in Figure 1C. The length of the nano-leaves ranges from 100 to 500 nm, and the width of each nano-leaf is approximately 50 nm. In order to verify the crystallographic quality, transmission electron microscopy (TEM) characterization was performed on individual nano-leaves. Figures 1D and E confirm that the nano-leaves are single crystals and tend to align along the [020]

direction. The high-resolution TEM (HRTEM) image (Figure 1F) and the corresponding filtered inverse fast Fourier transform (FFT) (Figure 1G) reveal that there are almost no dislocations in the observed regions of the nanostructures. Our XRD study (Figure S1) indicates that a two-hour calcination of the hydrothermal product is required to achieve phase-pure Ca_2CuO_3, whereas halving the calcination time leaves impurities such as CaO and CuO. Details of the chemical reaction process can be found in Supporting Information (SI).

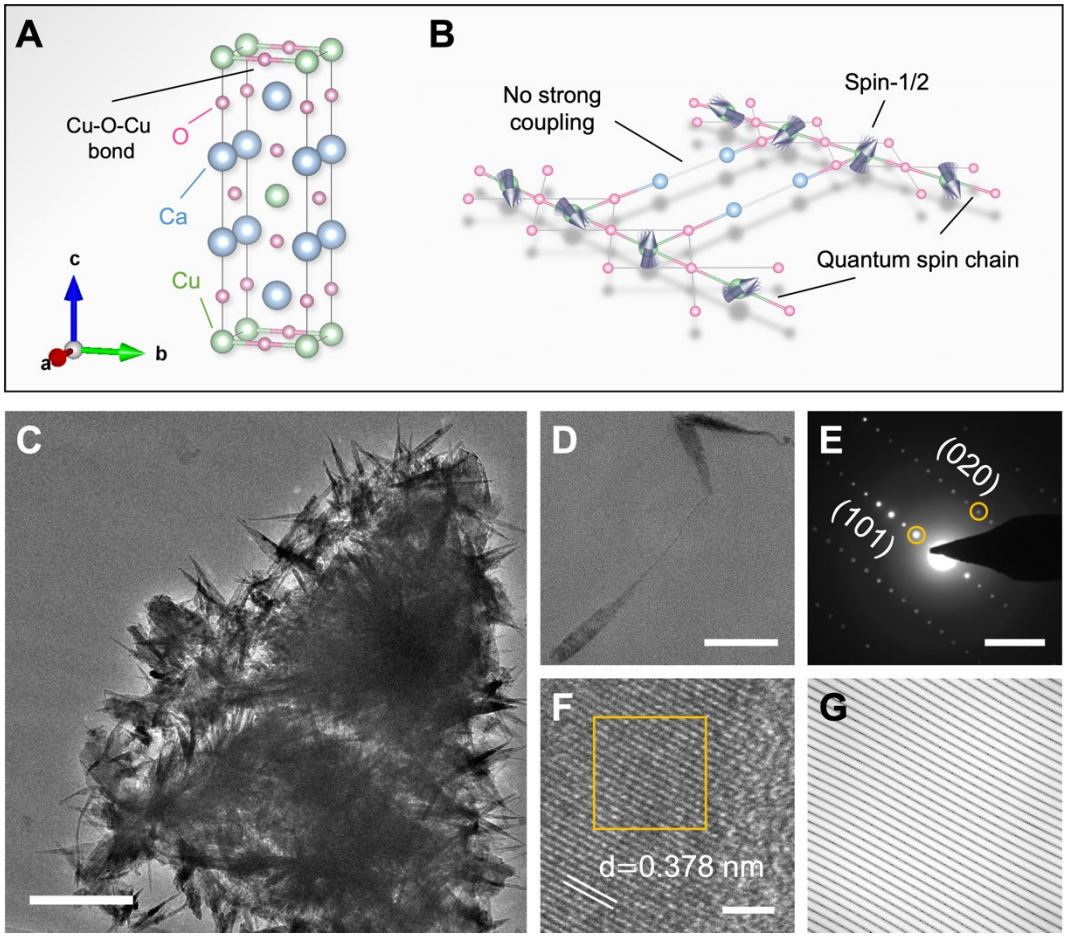

Figure 1: *(A) Crystal structure of Ca_2CuO_3. (B) Schematic diagram of quantum spin chains in Ca_2CuO_3, which lie along the b-axis and consist of Cu^{2+} ions sharing O^{2-} ions. (C) Bright-field TEM image of nano-leaves clustered together. The scale bar is 500 nm. (D) Bright-field TEM image of a nano-leaf. The scale bar is 300 nm. (E) Selected area electron diffraction pattern. The scale bar is 5 nm^{-1}. (F) High-resolution TEM image. The scale bar is 2 nm. (G) Corresponding filtered inverse FFT of the square area marked in (F).*

2.2 Alignment of Spin Chains

The obtained Ca_2CuO_3 nanostructures were consolidated into a pellet using the SCCP technique. For comparison, another pellet was prepared by the regular CP method. Figures 2A-C show that the layered grains in the SCCP sample are oriented predominantly in the plane perpendicular to the pressing direction. To quantify the grain orientations, XRD analyses were performed in both the in-plane (IP) and out-of-plane (OP) directions. As shown in Figure 2D, the (110) and (020) peaks are enhanced in the IP direction, while in the OP direction, diffraction peaks containing the b-axis contribution almost disappear, and the $(00l)$ peaks are strengthened significantly. In contrast, no clear difference was observed for the IP and OP directions for the CP sample (Figure S2). We further calculated the orientation factor (F) for the OP direction using the following equations:[43]

$$F = \frac{P-P_0}{1-P_0}, \quad (1)$$

$$P = \frac{\sum I(h0l)}{\sum I(hkl)}, \quad (2)$$

$$P_0 = \frac{\sum I_0(h0l)}{\sum I_0(hkl)}, \quad (3)$$

where $I(hkl)$ and $I_0(hkl)$ represent the measured and expected relative intensity values of the (hkl) planes, separately. P and P_0 are the ratios of the integrated intensities of all $(h0l)$ planes to the intensities of all (hkl) planes for preferentially and randomly oriented samples, respectively. For comparison, the F values for the (110) and (020) planes have been calculated in the IP direction. As listed in Table. 1, $F_{\mathrm{OP}}(h0l)$ of the SCCP sample is close to 1, demonstrating that there are almost no spin chains aligned along the OP direction. Additionally, the fact that the values of $F_{\mathrm{IP}}(110)$ and $F_{\mathrm{IP}}(020)$ are around 0.1 suggests that the b-axis has a preferential orientation in the IP direction. In contrast, F values are nearly 0 for the CP sample, indicating no distinct texture.

Table 1. *Calculated orientation factors of Ca_2CuO_3 based on XRD results*

Orientation Factor	Powder	SCCP-IP	SCCP-OP	CP-IP	CP-OP
$F(h0l)$	0.00	/	0.97	/	0.03
$F(110)$	0.00	0.12	/	0.00	/
$F(020)$	0.00	0.08	/	0.01	/

To better understand the anisotropic behavior, Raman spectra recorded from the SCCP sample

are given in Figure 2E. Along the IP direction, the observed peak positions agree well with previous Raman studies and reflect vibrational modes from the a-, b-, and c-axes.[44–46] Peaks with frequencies above 685 cm^{-1} are attributed to multi-phonon scattering. In addition, a broad peak around 2200 cm^{-1} is evident, indicating the presence of spinon-spinon pair states.[28,47] However, along the OP direction, the peaks associated with the a- and c-axes (308 and 532 cm^{-1}) are markedly intensified, while other peaks are strongly suppressed. In particular, the broad peak at 2200 cm^{-1} is nearly absent. This observation further implies that the grains are oriented predominantly with spin chains perpendicular to the OP direction. This preferred orientation is achieved due to the crucial steps in the SCCP process (Figure 2F). Initially, sustained high-speed stirring disperses the aggregated nano-leaves in the liquid, where surface tension causes them to unfold. Their high aspect ratio allows the long axes of the nano-leaves to remain horizontal. The pressure from the evaporating liquid further aligns and densifies the nano-leaves.[48,49] The final annealing process at 900 °C intensifies atomic motion, causing the interfaces between adjacent leaves to vanish, resulting in a denser, more uniform layered structure.[50,51]

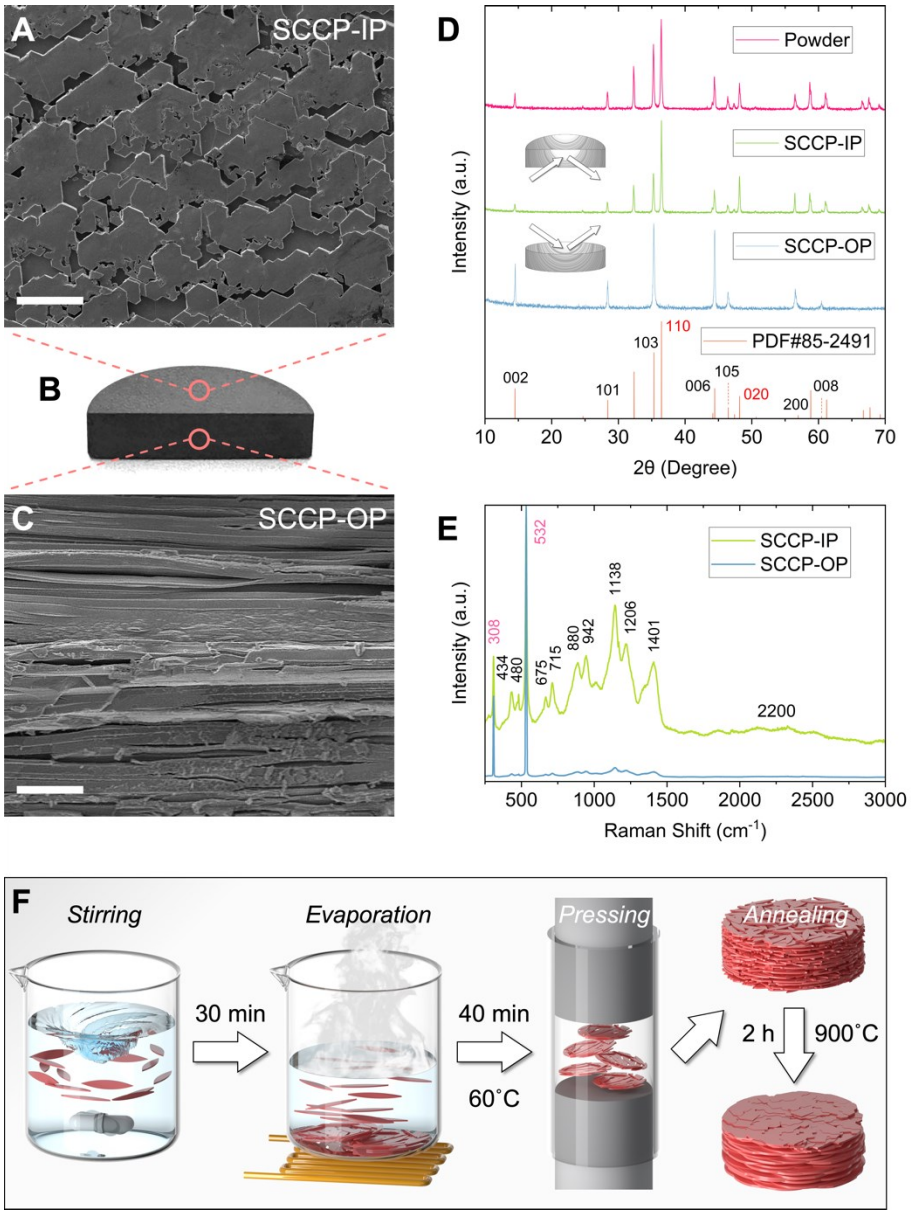

Figure 2: *(A-C) From top to bottom: SEM image recorded from a plane oriented along the IP direction, optical photograph, and SEM image recorded from a plane oriented along the OP direction of the SCCP sample. The scale bar in (A) is 1 μm. The scale bar in (C) is 5 μm. (D) XRD patterns recorded from Ca_2CuO_3 nano-leaves post-calcination and after the SCCP process in the IP and OP directions. (E) Raman spectra recorded from the IP and OP directions of the SCCP sample, excited by a 532-nm laser. (F) Essential steps in the SCCP method for preparing highly textured polycrystals.*

2.3 Thermal Conductivity and Spinon Contribution

As shown in Figure 3A, the specific heat (C_p) values of the two Ca_2CuO_3 samples coincide closely, demonstrating high similarity to a previous study.[28] The fitting of C_p within the range of 5-15 K

leads to a Debye temperature (θ_D) of 513 ± 3 K and J/k_B of 2068 ± 27 K, both close to the reported values of 521 K[28] and 2000 K[16], respectively. The detailed fitting procedure is presented in SI. Additionally, the Seebeck coefficient values of the SCCP and CP samples are highly consistent (Figure S3), suggesting that the two samples have similar hole concentrations.[52,53]

Figure 3B shows the T-dependence of κ measured from the samples in both the IP and OP directions from 3 to 350 K. Details about the uncertainty analysis are available in SI. For the SCCP sample, the κ within the plane orthogonal to the pressing direction is nearly isotropic. Intriguingly, above 75 K, the κ values for the SCCP sample exhibit significant anisotropy between the IP and OP directions, with κ^{IP} being much larger than κ^{OP}, and the aspect ratio approaching 4.5 above 300 K (Figure 3C). Conversely, the CP sample exhibits nearly isotropic behavior, with only a slight deviation above 75 K, while the aspect ratio remains around 1. The κ^{IP} value of the CP sample is also smaller than that of the SCCP sample. Compared with previously reported polycrystalline quantum magnets,[23,24,54–61] κ^{IP} of the SCCP sample is the highest at approximately 300 K (Figure 3D). Meanwhile, Figure 3E shows that the aspect ratio of κ is noticeably greater than that of most other single-phase polycrystalline materials.[23,24,50,62–68] The large and anisotropic κ is preferred for thermal management in microelectronic devices, as shown in Figure S4.

To eliminate the impact of porosity (Φ), with Φ_{SCCP} =21% and Φ_{CP} =22%, the Maxwell-Eucken relation can be employed:[69,70]

$$\kappa = \kappa_{\mathrm{solid}} \cdot \frac{\kappa_{\mathrm{p}}+2\kappa_{\mathrm{solid}}+2\Phi(\kappa_{\mathrm{p}}-\kappa_{\mathrm{solid}})}{\kappa_{\mathrm{p}}+2\kappa_{\mathrm{solid}}-\Phi(\kappa_{\mathrm{p}}-\kappa_{\mathrm{solid}})}, \quad (4)$$

where κ_{solid} represents the solid thermal conductivity, and κ_{p} is the pore thermal conductivity. Given that our measurements were conducted under ultra-high vacuum, κ_{p} is 0. Further details about the correction for the porosity effect are provided in SI. Since Ca_2CuO_3 is an insulator,[16] heat can only be carried by lattice vibrations and spin excitations, with lattice thermal conductivity (κ_l) being relatively isotropic along the three crystallographic axes according to the first-principles calculations.[28] Considering that spinon transport occurs solely along the 1D spin chains,[71] it follows that κ along the b-axis is larger than that along the other two axes, due to the spinon contribution. As illustrated in Figure 3F, the κ of single crystals perpendicular to the spin chains (κ^a and κ^c) exhibits similar values and T-dependence.[28] However, κ along the chains (κ^b) is much higher above 75 K. This deviation aligns closely with the anisotropy observed in the SCCP

sample. In combination with the calculated values of F, the high aspect ratio of κ can be attributed to κ_s being pronounced in the IP direction but negligible in the OP direction.

For the SCCP sample, given the similar values of κ^{IP} and κ^{OP} below 20 K (Figure S5), where κ_s is negligible due to the low population of spinons,[3,13,29] κ_l can be considered isotropic. Therefore, the spinon contribution along the IP direction (κ_s^{IP}) of the SCCP sample can be expressed as:

$$\kappa_s^{\mathrm{IP}} = \kappa^{\mathrm{IP}} - \kappa^{\mathrm{OP}}. \quad (5)$$

A detailed derivation of Equation 5 can be found in SI. As shown in Figure 3G, κ_s^{IP} is nearly identical in two orthogonal directions, exhibiting a broad peak and reaching a maximum of 22 $\mathrm{Wm^{-1}K^{-1}}$ around 120 K. This behavior arises because, at low T, the specific heat of spin excitations increases linearly with T due to the growth in the spinon population.[18] Meanwhile, boundary and defect scattering remain T-independent, causing κ_s to increase as T rises. However, at higher T, phonon excitations become significant, and T-dependent spinon-phonon scattering intensifies. This enhanced scattering reduces l_s, thereby suppressing κ_s. Consequently, κ_s exhibits a peak at a specific T. Additionally, defects can effectively break the chains into finite segments, introducing a spin gap,[13] which may result in the peak position shifting to a higher T. In addition, κ_s of the CP sample (Figure S6) shows a similar T-dependence to that observed in the SCCP sample but with a magnitude only about 2/3 as large. More significantly, the magnetic contribution of the SCCP sample, measured at 10 ± 1 $\mathrm{Wm^{-1}K^{-1}}$ at 300 K (Figure 3D), is the largest among all reported polycrystalline quantum materials, even exceeding the total κ of most polycrystalline quantum magnets. This arises because, spinon transport in the SCCP sample is confined to the 2D plane orthogonal to the pressing direction, whereas in the CP sample, it extends into 3D space, thereby dispersing approximately 1/3 of the spinon contribution along the OP direction.

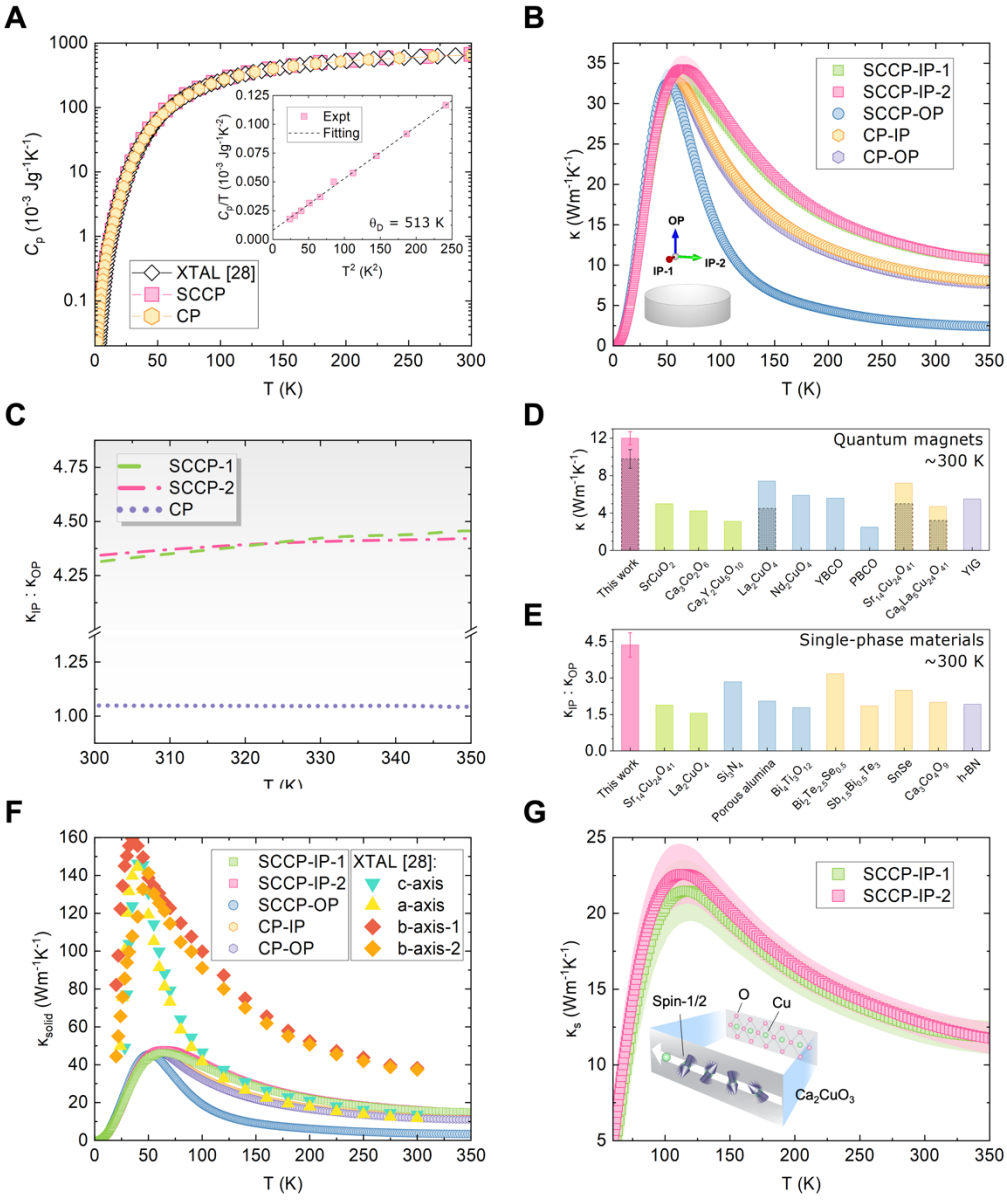

Figure 3: *(A) T-dependence of C_p for the two samples in comparison with the single-crystal data reported by Chen et al.*[28] *Inset: relationship between $C_p(T)/T$ and T^2. The black dashed line is a fitting curve. Error bars are included but are too small to be visible. (B) T-dependence of κ for the two samples measured in the IP and OP directions. The shaded area depicts the measurement error. (C) T-dependence of the aspect ratio of κ for the two samples above 300 K. (D) Comparison of κ between the SCCP sample and previously reported polycrystalline quantum magnets at around 300 K (Spin chain: $SrCuO_2$,*[54] *$Ca_3Co_2O_6$,*[55] *$Ca_2Y_2Cu_5O_{10}$;*[56] *Spin plane: La_2CuO_4,*[24] *Nd_2CuO_4,*[57] *YBCO,*[58] *PBCO;*[59] *Spin ladder: $Sr_{14}Cu_{24}O_{41}$,*[23] *$Ca_9La_5Cu_{24}O_{41}$;*[60] *Ferrite: YIG*[61]*). The shaded area represents the spin-mediated κ. (E) Comparison of aspect ratio of κ between the SCCP sample and other previously reported polycrystalline single-phase materials, at around 300 K (Magnetic material: $Sr_{14}Cu_{24}O_{41}$,*[23] *La_2CuO_4;*[24] *Ceramics: Si_3N_4,*[62] *Porous alumina,*[63] *$Bi_4Ti_3O_{12}$;*[64] *Thermoelectric material: $Bi_2Te_{2.5}Se_{0.5}$,*[50]

$Sb_{1.5}Bi_{0.5}Te_3$,[65] SnSe,[66] $Ca_3Co_4O_9$;[67] Van der Waals material: h-BN[68]). (F) Comparison between κ_{solid} of two samples with single-crystal data along the a-, b-, and c-axes.[28] (G) *T-dependence of κ_s^{IP} for the SCCP sample in two orthogonal directions. Inset: schematic diagram of spinon thermal transport along Cu-O-Cu bonds in Ca_2CuO_3. The shaded area depicts the estimated uncertainty of κ_s.*

2.4 Analysis of Spinon Thermal Transport

To better understand spinon transport in polycrystals, the intrinsic spinon thermal conductivity (κ_s^i) of the SCCP polycrystal was compared with reported single-crystal data.[28] κ_s^i can be obtained from:

$$\kappa_s^i = 3\left(\kappa^{poly} - \kappa_l^{poly}\right) = 3\kappa_s^{poly} = \kappa^{\text{IP}-1} + \kappa^{\text{IP}-2} - 2\kappa^{\text{OP}}, \quad (6)$$

where κ_l^{poly} and κ_s^{poly} represent the lattice and spinon thermal conductivities of a polycrystal with randomly distributed grains, respectively. The proof of Equation 6 can be found in SI. As shown in Figure 4A, the polycrystal shows a similar T-dependence to single crystals,[28] with the peak shifting from 90 K in single crystals to 110 K in the polycrystal. This shift can be attributed to stronger spinon-defect scattering in the polycrystal. Interestingly, although there is a notable decrease in κ_s^i from single crystals to the polycrystal at low T, the values of κ_s^i at high T are almost identical. Moreover, κ_s^i of the CP sample overlap perfectly with that of the SCCP sample, suggesting that the intrinsic spinon contribution is unaffected by texturing. The process for obtaining κ_s^i of the CP sample is detailed in SI.

The average spinon MFP, l_s, for $T \ll J/k_B$ was calculated through a kinetic model for 1D spinon transport:[17,29,72]

$$l_s = \frac{3\hbar\kappa_s^i}{\pi N_s k_B^2 T}, \quad (7)$$

where $N_s = 2/ac$ is the number of spin chains per unit area. Here, a =3.28 Å and c =12.28 Å are the lattice constants of the a- and c-axes, respectively. As shown in Figure 4B, at 100 K there is a clear difference in l_s of 510~600 Å for single crystals compared to 440 Å for polycrystals. With increasing T, l_s for all of the samples decreases, converging to a constant value of 90 Å at 300 K. In 1D spin chains, spinon thermal transport is primarily limited by two scattering mechanisms: coupling of spinons with phonons (l_{sp}), which affects spinon thermal transport by perturbing the Cu-O-Cu separation, thereby altering J,[73] and scattering of spinons by defects (l_d),

which are due to breaks in the spin chains.[3] According to Matthiessen's rule, l_s can be expressed as:

$$l_s^{-1} = l_{sp}^{-1} + l_d^{-1}. \quad (8)$$

The T-dependence of l_{sp} can be described as:[3]

$$l_{sp}^{-1} = g_{sp}^2 \cdot \frac{2J}{k_B T a} \cdot \frac{1}{\sinh(2\pi\hbar\varpi_0/k_B T)}, \quad (9)$$

where g_{sp} is the spinon-phonon coupling constant, J/k_B is set to 2000 K, and ϖ_0 represents the frequency of the phonon mode. Based on previous theoretical and inelastic neutron scattering studies,[3,28,74] spinons primarily interact with two optical phonon modes with energies around 25 and 78 meV. Therefore, l_{sp} can be described as:

$$l_{sp}^{-1} = l_{sp-1}^{-1} + l_{sp-2}^{-1}, \quad (10)$$

where l_{sp-1} and l_{sp-2} are the MFP of spinons coupled with low- and high-frequency phonons, respectively. For spinon-defect scattering, l_d represents the average distance between two neighboring breaks:[3]

$$l_d^{-1} = n_d, \quad (11)$$

where n_d is the concentration of breaks in 1D spin chains. The experimental l_s values can be well fitted utilizing Equations 8-11. The fitting parameters are listed in Table. 2. g_{sp-1} and g_{sp-2} are close between the SCCP polycrystal and single crystals, and are both much smaller than 1, indicating weak spinon-phonon coupling in 1D spin chains.[3,74] Furthermore, in the SCCP sample, the average grain size, around 500 nm, greatly exceeds l_d. Therefore, spinon-defect scattering dominates over spinon-boundary scattering due to its relatively higher scattering rate, more effectively limiting l_s. Additionally, in the 1D antiferromagnetic spin-chain compound Ca_2CuO_3, grain boundaries behave similarly to point defects, as both introduce disorder and disrupt spinon heat transport by breaking the continuity of the spin chains, thereby suppressing κ_m. Consequently, n_d includes the contributions not only from impurities and dislocations but also from grain boundaries. The well-aligned fitting curve for l_s of the SCCP sample in Figure 4B, modeled using Equations 8–11, further supports this perspective.

Table 2. *Fitting parameters for spinon MFP*

Sample	g_{sp-1}	g_{sp-2}	n_d (Å^{-1})

b-axis-1	0.023 ± 0.001	0.16 ± 0.002	0.00099 ± 0.00002
b-axis-2	0.025 ± 0.001	0.16 ± 0.002	0.00115 ± 0.00004
SCCP	0.024 ± 0.001	0.16 ± 0.002	0.00148 ± 0.00003

To verify the reliability of our analysis, we also estimated n_d of the SCCP sample using C_p measurements. At low T, in the presence of uncompensated spin 1/2 at the ends of fragmented chain segments, the Schottky contribution can result in abnormal deviations in C_p for Ca_2CuO_3 in different magnetic fields (Figure 4C).[75,76] This phenomenon occurs because non-stoichiometry at copper or oxygen sites or impurity phases can break a 1D spin-chain into several segments of even and odd length, each containing a corresponding even or odd number of Cu sites. Due to the presence of both even-length and odd-length segments, the average concentration is ~$0.5n_d$. The odd-length chains can contribute an additional term to C_p at low T, described by the Schottky specific heat:[77]

$$C_{\mathrm{Sch}} = \left[\left(\frac{n_d}{2}\right)\cdot R\cdot\left(\frac{\Delta_g}{T}\right)^2\cdot e^{\left(\frac{\Delta_g}{T}\right)}\right]\Big/\left[1+e^{\left(\frac{\Delta_g}{T}\right)}\right]^2, \quad (12)$$

where Δ_g is the energy level splitting, and R is the ideal gas constant. By analyzing the difference in specific heat (ΔC_p) measured at two different magnetic fields ($C_{p,\mathrm{H}}$), n_d can be determined from the expression:

$$\Delta C_p = C_{p,\mathrm{H}_1} - C_{p,\mathrm{H}_2},\ (\mathrm{H}_1 < \mathrm{H}_2) \quad (13)$$

which effectively minimizes the effects of lattice and spinon contributions.[75] A combination of Equations 12 and 13 is used to fit the ΔC_p data, with n_d and Δ_g as fitting parameters in different magnetic fields (Figure 4D). Details of the fitting process can be found in SI. The derived values are n_d =0.0057 ± 0.00005 per Cu, Δ_g=1.1 ± 0.02 K at 5 T, and Δ_g=24.6 ± 0.4 K at 9 T. Given that the lattice constant of the b-axis determined from the XRD results is 3.78 Å, n_d =$0.0057/b$ =0.0015 ± 0.00002 Å^{-1}, which agrees well with the n_d value obtained from l_s analysis.

To better understand the impact of different scattering processes on spinon thermal transport, we calculated the T-dependence of l_s at different n_d using Equations 8-11. As shown in Figure S7A, increasing n_d leads to a decrease in l_s at low T while leaving it almost unchanged at high T. However, when the impact of spinons coupling with high-frequency phonons is removed, l_s

becomes strongly dependent on n_d at both low and high T. To further investigate the origin of this behavior, we calculated κ_s for various scattering processes as a function of l_d using Equations 7-11. As illustrated in Figure 4E, at 100 K, when all scattering processes are considered, κ_s reduces with decreasing l_d, matching the experimental values well. Omitting l_{sp-2} has little effect on κ_s, but excluding the contribution from l_{sp-1} leads to a large deviation from the experimental results. Therefore, at low T, both spinon-defect scattering and coupling of spinons with low-frequency phonons predominantly govern spinon thermal transport in 1D spin chains, while coupling between spinons and high-frequency phonons is negligible. Conversely, at 300 K, κ_s remains essentially constant regardless of whether l_{sp-1} is considered (Figure 4F). Only when $l_d < 300$ Å, approximately 80 lattice spacings of the b-axis, does κ_s begin to show a strong dependence on l_d. However, removing l_{sp-2} results in significant deviation from the experimental data. Thus, at high T, the similar values of κ_s for single crystals and polycrystalline samples can be attributed to dominant coupling between spinons and high-frequency phonons. Moreover, as shown in Figure S7B, which illustrates the calculated T-dependence of κ_s with and without n_d included through Equations 7-11, the calculated values align closely with the experimental data above 250 K, regardless of n_d. However, the curve excluding n_d deviates significantly from the experimental data below 150 K, confirming that spinon-defect scattering is crucial at low T but has minimal effect at high T. This phenomenon occurs because only low-frequency phonons are significantly excited at low T. As T increases, high-frequency phonons become more populated and can frequently couple with spinons, thereby suppressing the impact of spinon-defect scattering.[3]

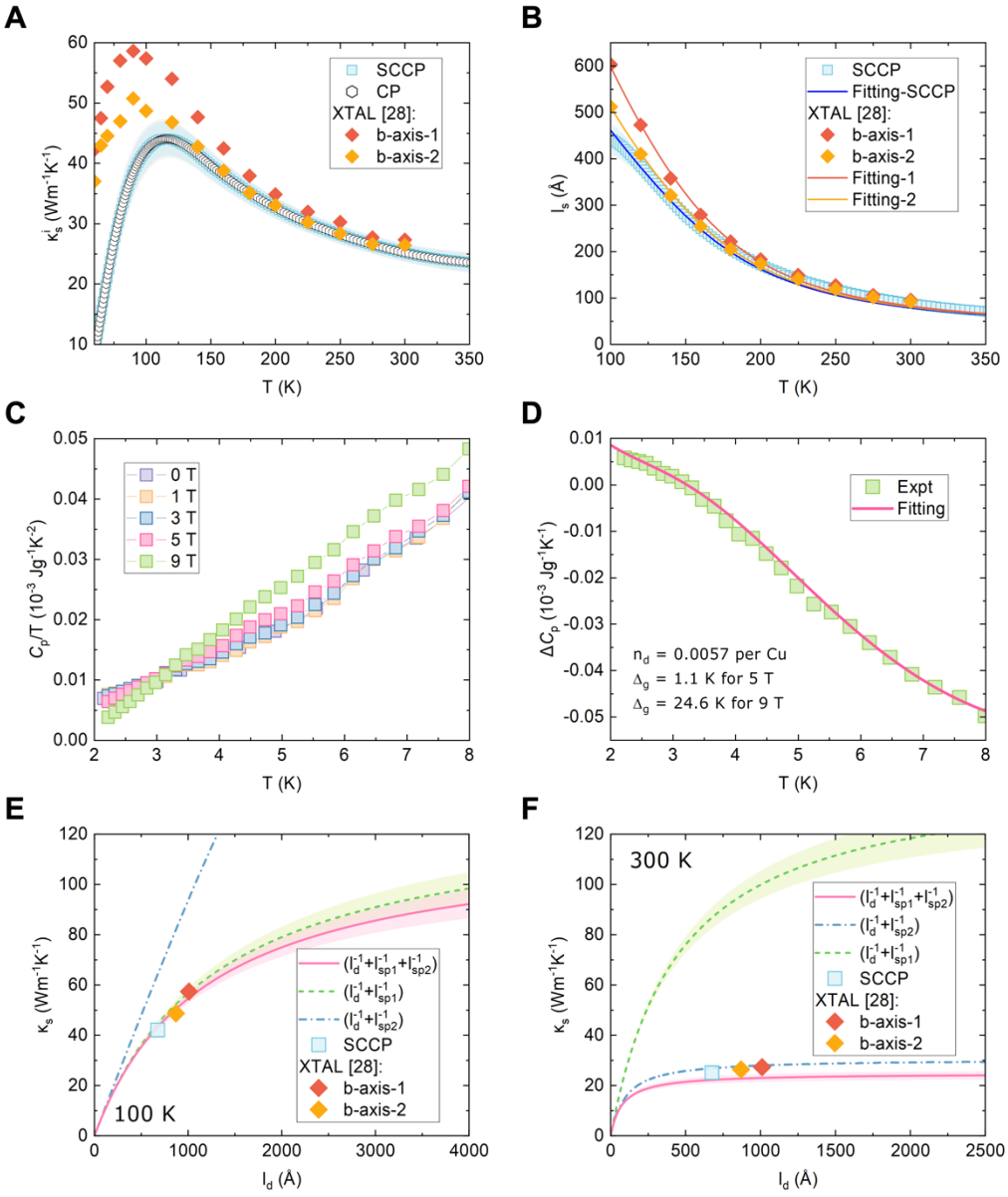

Figure 4: *(A) T-dependence of* κ_s^i *for two polycrystals, shown together with single-crystal data reported by Chen et al.*[28] *(B) T-dependence of* l_s *for the SCCP polycrystal, shown together with single-crystal data.* κ_s^i *used for the calculation was obtained from (A). The solid lines are fitting curves based on Equations 8-11. (C) T-dependence of* $C_p(T)/T$ *under various applied magnetic fields. Error bars are included but are too small to be visible. (D) Specific heat difference* ΔC_p *obtained by subtracting* C_p *under fields of 5 and 9 T. The pink line is a fitting curve. (E) and (F) Calculated and experimental* κ_s*, plotted as a function of* l_d *at 100 and 300 K, respectively. The shaded area depicts the calculation error for* κ_s^i.

2.5 Anisotropic Magnon Thermal Transport in Textured La_2CuO_4 Prepared using the SCCP Method

To demonstrate the broad applicability of the SCCP method, we applied it to synthesize textured quantum magnet La_2CuO_4 with large anisotropic κ_m. 1D La_2CuO_4 nano-rods grown through a wet chemical method[24] were consolidated into a textured pellet using the SCCP method. The SEM image (Figure S8) shows that the La_2CuO_4 nano-rods tend to align perpendicularly to the pressing pressure. The XRD patterns (Figure 5A) show that the $(0k0)$, (200) and (220) peaks are enhanced in the IP direction, while they nearly vanish in the OP direction. La_2CuO_4 has a 2D magnetic structure (Figure S9), where magnons transport uniformly in the spin-plane (ab-plane) but disappear along the c-axis.[78,79] The F value of $(hk0)$ for the IP direction, calculated using Equations 1-3, is 0.4, suggesting that magnons preferentially exist and propagate in this direction. As shown in Figure 5B, at room-temperature, κ of the textured La_2CuO_4 in the IP direction is improved by approximately 30% compared to the sample prepared via spark plasma sintering (SPS), whereas κ in the OP direction is halved.[24] Using the Debye-Callaway model, κ_l was estimated to isolate the magnon contribution. The fitting details are provided in SI. Figure 5C illustrates that at 300 K, the magnon contribution of the SCCP sample is intensified by nearly 40% in the IP direction, while in the OP direction, it is attenuated to 2/5 of the SPS sample. Thus, the spin-mediated thermal transport in the La_2CuO_4 sample prepared by the SCCP method exhibits strong directional behavior and pronounced anisotropy, with an aspect ratio of κ_m around 5, more than triple the 1.5 in the SPS sample (Figure 5D).

To better understand magnon transport in textured La_2CuO_4, the intrinsic magnon thermal conductivity (κ_m^i) of the SCCP polycrystal was calculated and compared with reported single-crystal data.[20] Details of the calculation process are provided in SI. As shown in Figure 5E, κ_m^i of La_2CuO_4 increases with T, in contrast to the behavior of Ca_2CuO_3. At low T, κ_m^i values for the single-crystal and SCCP sample are nearly identical; however, a notable difference emerges at high T. We further calculated the average magnon MFP (l_m) using a kinetic model for 2D magnon transport,[13,20,35] with details in SI. As seen in Figure 5F, l_m decreases with T, with a widening gap between the two samples at elevated T. To investigate the origin of the suppressed κ_m^i and l_m values in the SCCP sample, we calculated the T-dependent l_m across different defect concentrations. Figure S10A demonstrates that increasing defect concentration slightly reduces l_m at low T, with a more pronounced at higher T. This finding is attributed to frequency-dependent magnon-defect scattering,[24,80] which increases the defect scattering rate with rising T, thus more

effectively suppressing l_m. This observation contrasts with Ca_2CuO_3, where defect scattering remains T-independent. Incorporating boundary scattering and frequency-dependent defect scattering in La_2CuO_4, we achieved good agreement between the experimental l_m results and the model (Figure 5F), with the fitting process described in SI. Additionally, Figure S10B shows the calculated κ_m with and without defect scattering, verifying its significant impact at high T.

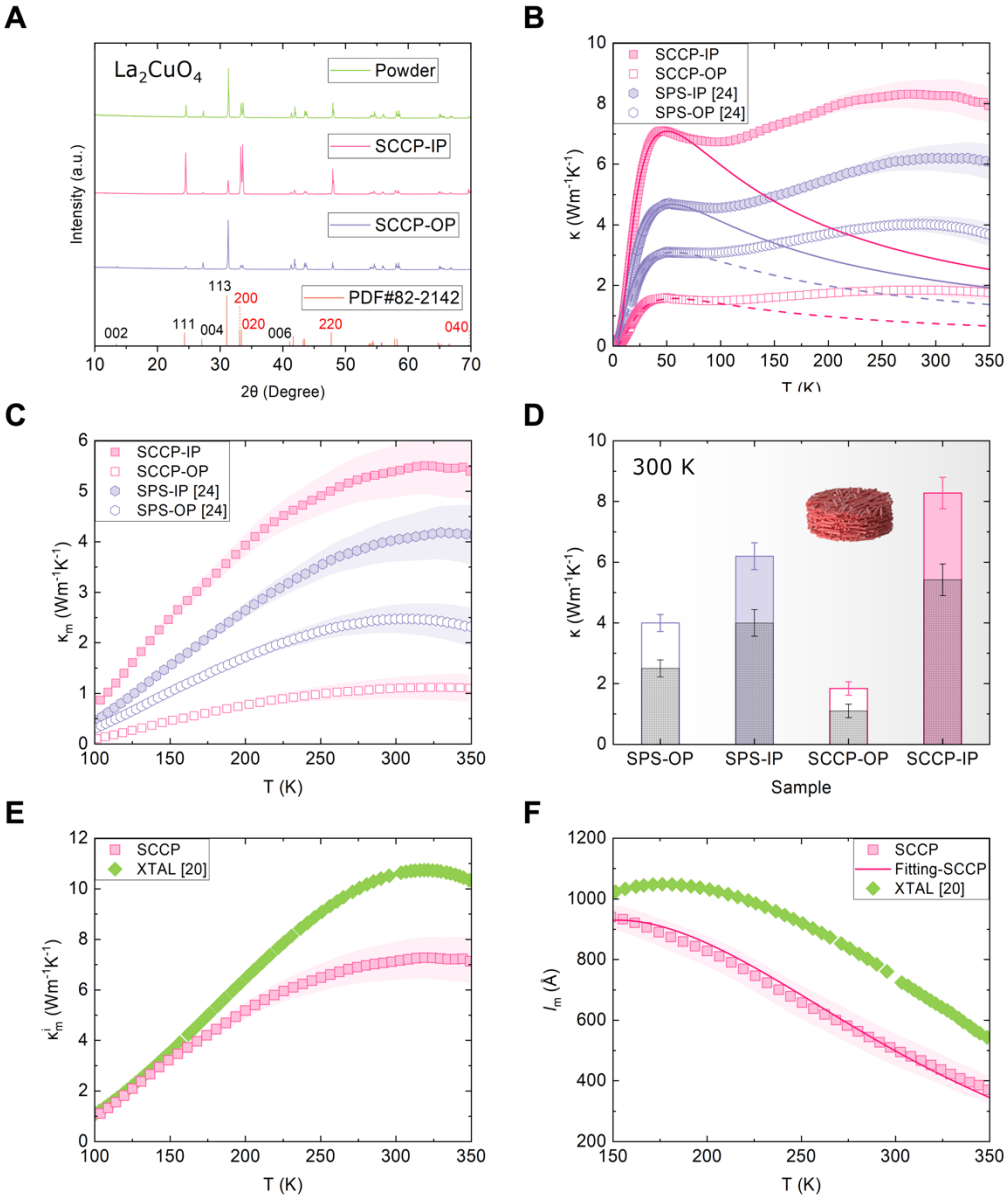

Figure 5: *(A) XRD patterns of the SCCP sample recorded from the IP and OP directions. (B) κ of the SCCP sample obtained from the IP and OP directions, in comparison with the SPS sample.*[24] *The shaded area depicts the measurement error. The solid and dashed lines are fitted κ_l based on the Debye-Callaway model. (C) T-dependence of κ_m for the SCCP sample, shown together with the SPS sample.*[24] *The shaded area depicts the estimated uncertainty of κ_m. (D) Comparison of κ and κ_m between the SCCP and SPS samples obtained from the IP and OP directions at 300 K. The shaded areas represent κ_m. Inset: schematic diagram of the distribution of La_2CuO_4 nano-rods in the SCCP sample. (E) T-dependence of κ_m^i for the SCCP polycrystal, shown together with*

single-crystal data reported by Hess et al.[20] *The shaded area depicts the estimated uncertainty of* κ_m^i. *(B)* T*-dependence of* l_m *for the SCCP polycrystal, shown together with single-crystal data.*[20] *The shaded area depicts the estimated uncertainty of* l_m.

When comparing Ca_2CuO_3 and La_2CuO_4 prepared through SCCP, we identified a key difference in the thermal transport mechanisms of spin excitations: the dominant role of defects varies across different T ranges. In Ca_2CuO_3, a 1D spin-chain system, defects primarily govern spinon thermal transport at T below 150 K. As defect concentration increases, κ_s is effectively suppressed. However, at high T, this effect is overtaken by strong coupling between spinons and high-frequency phonons. A similar phenomenon has been observed in single-crystal Sr_2CuO_3,[5] another 1D spin-chain compound. In contrast, for La_2CuO_4, a 2D spin-plane system, defect scattering primarily dominates magnon thermal transport at high T, especially above 250 K, where a high concentration of defects significantly reduces κ_m. This effect is much less pronounced at low T, with comparable behavior has been detected by other groups in polycrystalline[20] and single-crystal[81] La_2CuO_4. Additionally, in quasi-1D spin-ladder systems, where spins are arranged in two parallel chains connected by rungs to form a ladder-like structure,[82] magnon-defect scattering plays an important role at intermediate T, particularly between 100 and 200 K, as reported in polycrystalline[23] and single-crystal $Sr_{14}Cu_{24}O_{41}$,[27] as well as in single-crystal $Ca_9La_5Cu_{24}O_{41}$.[27] In these three spin systems, defects play a critical role across different T ranges possibly due to variations in their spin structures, spin gap sizes, and types of spin excitations. Further theoretical studies are needed to better understand the mechanisms of defect scattering in these quantum magnetic systems.

3. Conclusion

A simple solvent-cast cold pressing method was developed and used to successfully prepare a highly textured spin-chain compound Ca_2CuO_3, aligning the 2D nanostructures with spin chains perpendicular to the pressing direction. As a result, we realized a high room-temperature κ of 12 ± 0.7 W m^{-1} K^{-1}, surpassing all polycrystalline quantum magnets. This result can be attributed to its substantial spin-mediated κ of 10 ± 1 W m^{-1} K^{-1}, which is the highest among all polycrystalline quantum materials. Furthermore, the aspect ratio of κ rises to about 4.5 above 300 K, close to the maximum value reported for single-phase polycrystalline materials. This behavior is attributed to the strong and anisotropic spinon thermal transport in the highly textured sample, produced by

pressing nano-leaves using the SCCP method. The procedure requires only 4 hours at 900 ˚C, which is only 1/15 of the time required for single-crystal preparation. The grains in the textured sample are aligned with the spin chains perpendicular to the pressing direction. Therefore, κ_s is significantly enhanced along the IP direction, being about 1.5 times greater than that of a reference polycrystal prepared using a traditional CP procedure. Based on our theoretical analysis, spinon thermal transport at room-temperature is dominated by coupling of spinons with high-frequency phonons, while extrinsic spinon-defect scattering is negligible if n_d is smaller than 0.003 $Å^{-1}$. As a result of this unique feature, polycrystalline spin-chain compounds are promising candidates for achieving large κ_s close to room-temperature. Additionally, we demonstrated that this SCCP method can be applied to prepare textured quantum magnet La_2CuO_4 with large anisotropic magnon thermal transport, where the aspect ratio of κ_m is more than 3 times that of the sample prepared by SPS, showcasing its broad versatility. In addition, we observed distinct role of defect scattering on spin-mediated thermal transport in 1D spin-chain, quasi-1D spin-ladder, and 2D spin-plane systems. Our results not only provide valuable insight into spin-mediated thermal transport mechanisms in polycrystals but also open new avenues for designing textured quantum materials for thermal management and energy conversion.

4. Experimental Section

4.1 Material Synthesis

Ca_2CuO_3 nano-leaves were synthesized using a wet chemical method that involves hydrothermal treatment followed by calcination. In a typical procedure, 1.24 g of $Ca(NO_3)_2{\cdot}4H_2O$ (purity $\geq$ 99.99%) and 0.42 g of $Cu(NO_3)_2{\cdot}2.5H_2O$ (purity $\geq$ 99.99%) were dissolved in 30 mL of deionized water under stirring and ultrasonic irradiation. Then, 10 mL of a 12 mol/L NaOH aqueous solution was added dropwise while stirring vigorously. The resulting co-precipitate was transferred to a 50 mL Teflon-lined stainless steel autoclave for hydrothermal treatment at 180 ˚C for 20 hours. After cooling to room-temperature, the suspension was removed, and the precipitate was mixed thoroughly with 40 mL of deionized water and then centrifuged. This process was repeated three times. The final sediment was mixed evenly with 20 mL of deionized water, filtered, and dried at 80 ˚C for 12 hours. The resulting powder was calcined in air, with a heating rate of 3 K/min from room-temperature to 900 ˚C and maintained at this temperature for 2 hours.

4.2 Solvent-Cast Cold Pressing

Tin foil was cut precisely to the required size and shape before being affixed to the bottom of the beaker. Then, Ca_2CuO_3 nano-leaves were dispersed in 50 mL of liquid. In order to prevent Ca_2CuO_3 from hydrating, acetone, with a lower boiling point (56 °C), was used. The solution was subjected to ultrasonic irradiation for 15 minutes, followed by magnetic stirring for 15 minutes to achieve a uniform dispersion. The mixture was placed in a drying oven set to 60 ˚C for 40 minutes. It is important to note that the drying duration is contingent on the complete evaporation of the acetone. The flaky precipitates were carefully peeled off from the tin foil and placed into a pellet pressing die set, layer by layer, in a horizontal orientation. They were then consolidated into a pellet by cold pressing at a pressure of 320 MPa. The obtained pellet was annealed at 900 ˚C for 2 hours.

Textured La_2CuO_4 was prepared following the same steps described above, with one modification: after cold pressing the pellet at a pressure of 320 MPa, it was annealed at 850 °C for 4 hours instead of 900 °C for 2 hours.

4.3 Material Characterization

The phase purity, crystal structure, and texture of the samples were analyzed using a PANalytical Empyrean Series 2 X-ray diffraction machine (Malvern Panalytical, Malvern, UK) equipped with Cu Kα radiation (λ = 1.54 Å). Raman measurements were performed at 300 K using a HORIBA LabRam equipped with a 532 nm laser.

Structural and compositional data of samples were collected using a ThermoFisher Scientific Talos L120C transmission electron microscope (TEM) and a ThermoFisher Scientific Titan Themis 300 scanning TEM (STEM). STEM analyses were conducted at 300 kV using an X-FEG electron source. High-resolution TEM images were captured using a 2048 x 2048 pixel FEI CETA-16 M CMOS digital camera, with a beam convergence semi-angle of 0.08 mrad. For morphological investigations, a TESCAN Vega3 SBH scanning electron microscope (TESCAN, Brno, Czech Republic) was operated at 10 kV.

The specific heat, thermal conductivity, and Seebeck coefficient of the samples were measured using a Quantum Design Physical Property Measurement System (PPMS) over a temperature range of about 2 to 350 K. Further information about the thermal conductivity measurements and

uncertainty analyses is available in SI.

Supporting Information

Supporting Information is available from the Wiley Online Library or from the author.

Acknowledgements

This work was supported by the National Science Foundation under grant 2144328.

Conflict of Interest

The authors declare no conflict of interest

Data Availability Statement

The data that support the findings of this study are available from the corresponding author upon reasonable request.

Reference

[1] S. Guo, Y. Xu, T. Hoke, G. Sohi, S. Li, X. Chen, *J Appl Phys* **2023**, 133, 120701.

[2] B. Zare Rameshti, S. Viola Kusminskiy, J. A. Haigh, K. Usami, D. Lachance-Quirion, Y. Nakamura, C.-M. Hu, H. X. Tang, G. E. W. Bauer, Y. M. Blanter, *Phys Rep* **2022**, 979, 1.

[3] A. L. Chernyshev, A. V. Rozhkov, *Phys Rev Lett* **2016**, 116, 017204.

[4] C. de Graaf, F. Illas, *Phys Rev B* **2000**, 63, 014404.

[5] N. Hlubek, X. Zotos, S. Singh, R. Saint-Martin, A. Revcolevschi, B. Büchner, C. Hess, *J Stat Mech* **2012**, 2012, P03006.

[6] Y. Saleem, T. Steenbock, E. R. J. Alhadi, W. Pasek, G. Bester, P. Potasz, *Nano Lett* **2024**, 24, 7417.

[7] M. Zeng, Y. Feng, G. Liang, *Nano Lett* **2011**, 11, 1369.

[8] D. Hirobe, M. Sato, T. Kawamata, Y. Shiomi, K. Uchida, R. Iguchi, Y. Koike, S. Maekawa, E. Saitoh, *Nat Phys* **2017**, 13, 30.

[9] A. Kapelrud, A. Brataas, *Phys Rev Lett* **2013**, 111, 097602.

[10] H. Hayashi, K. Ando, *Phys Rev Lett* **2018**, 121, 237202.

[11] A. Klümper, K. Sakai, *J Phys A: Math Gen* **2002**, 35, 2173.

[12] Th. Niemeijer, H. A. W. van Vianen, *Phys Lett A* **1971**, 34, 401.

[13] C. Hess, *Phys Rep* **2019**, 811, 1.

[14] X. Zotos, F. Naef, P. Prelovsek, *Phys Rev B* **1997**, 55, 11029.

[15] F. Heidrich-Meisner, A. Honecker, D. C. Cabra, W. Brenig, *Phys Rev B* **2003**, 68, 134436.

[16] K. Foyevtsova, J. T. Krogel, J. Kim, P. R. C. Kent, E. Dagotto, F. A. Reboredo, *Phys Rev X*

2014, 4, 031003.

[17] C. Hess, H. ElHaes, A. Waske, B. Büchner, C. Sekar, G. Krabbes, F. Heidrich-Meisner, W. Brenig, *Phys Rev Lett* **2007**, 98, 027201.

[18] A. V. Sologubenko, E. Felder, K. Giannò, H. R. Ott, A. Vietkine, A. Revcolevschi, *Phys Rev B* **2000**, 62, R6108.

[19] N. Hlubek, P. Ribeiro, R. Saint-Martin, A. Revcolevschi, G. Roth, G. Behr, B. Büchner, C. Hess, *Phys Rev B* **2010**, 81, 020405.

[20] C. Hess, B. Büchner, U. Ammerahl, L. Colonescu, F. Heidrich-Meisner, W. Brenig, A. Revcolevschi, *Phys Rev Lett* **2003**, 90, 197002.

[21] C. Hess, P. Ribeiro, B. Büchner, H. ElHaes, G. Roth, U. Ammerahl, A. Revcolevschi, *Phys Rev B* **2006**, 73, 104407.

[22] A. Mohan, N. S. Beesetty, N. Hlubek, R. Saint-Martin, A. Revcolevschi, B. Büchner, C. Hess, *Phys Rev B* **2014**, 89, 104302.

[23] X. Chen, K. Jarvis, S. Sullivan, Y. Li, J. Zhou, L. Shi, *Phys Rev B* **2017**, 95, 144310.

[24] S. Guo, H. Li, X. Bai, Y. Wang, S. Li, R. E. Dunin-Borkowski, J. Zhou, X. Chen, *Cell Rep Phys Sci* **2024**, 5, 101879.

[25] C. Hess, C. Baumann, B. Büchner, *J Magn Magn Mater* **2005**, 290–291, 322.

[26] M. Montagnese et al., *Phys Rev Lett* **2013**, 110, 147206.

[27] C. Hess, H. ElHaes, B. Büchner, U. Ammerahl, M. Hücker, A. Revcolevschi, *Phys Rev Lett* **2004**, 93, 027005.

[28] X. Chen, J. Carrete, S. Sullivan, A. van Roekeghem, Z. Li, X. Li, J. Zhou, N. Mingo, L. Shi, *Phys Rev Lett* **2019**, 122, 185901.

[29] A. V. Sologubenko, K. Giannò, H. R. Ott, A. Vietkine, A. Revcolevschi, *Phys Rev B* **2001**, 64, 054412.

[30] A. L. Moore, L. Shi, *Mater Today* **2014**, 17, 163.

[31] S. Shin, Q. Wang, J. Luo, R. Chen, *Adv Funct Mater* **2020**, 30, 1904815.

[32] L. Yang et al., *Nat Nanotechnol* **2021**, 16, 764.

[33] T. Li et al., *Sci Adv* **2018**, 4, aar3724.

[34] J. Han, G. Du, W. Gao, H. Bai, *Adv Funct Mater* **2019**, 29, 1900412.

[35] S. R. Boona, J. P. Heremans, *Phys Rev B* **2014**, 90, 064421.

[36] R. Jin, Y. Onose, Y. Tokura, D. Mandrus, P. Dai, B. C. Sales, *Phys Rev Lett* **2003**, 91, 146601.

[37] J. Paglione, N. P. Butch, E. E. Rodriguez, *World Scientific* **2021**.

[38] N. Terakado, R. Takahashi, Y. Takahashi, T. Fujiwara, *Appl Phys Lett* **2017**, 110, 191902.

[39] T. Kawamata, N. Takahashi, T. Adachi, T. Noji, K. Kudo, N. Kobayashi, Y. Koike, *J Physical Soc Japan* **2008**, 77, 034607.

[40] M. Hjorth, J. Hyldtoft, A. Mostad, C. Rømming, R. Salmén, H. H. Tønnesen, T. Tokii, *Acta Chem Scand* **1990**, 44, 516.

[41] J. des Cloizeaux, J. J. Pearson, *Physical Review* **1962**, 128, 2131.

[42] B. Lake, D. A. Tennant, C. D. Frost, S. E. Nagler, *Nat Mater* **2005**, 4, 329.

[43] F. K. Lotgering, *J. Inorg. Nucl. Chem* **1959**, 9, 113.

[44] M. Yoshida, S. Tajima, N. Koshizuka, S. Tanaka, S. Uchida, S. Ishibashi, *Phys Rev B* **1991**, 44, 11997.

[45] Ya. S. Bobovich, V. N. Denisov, B. N. Mavrin, T. I. Chuvaeva, *Opt Spectrosc* **2000**, 89, 372.

[46] S. Sugai, J. Wada, K. Yamada, S. Hosoya, Y. Endoh, *Physica B Condens Matter* **1996**, 219–

220, 505.
[47] O. V. Misochko, S. Tajima, C. Urano, H. Eisaki, S. Uchida, *Phys Rev B* 1996, 53, R14733.
[48] Y. Li, Y. Wu, *J Am Chem Soc* **2009**, 131, 5851.
[49] M. H. Modarres, S. Engelke, C. Jo, D. Seveno, M. De Volder, *Nano Lett* **2019**, 19, 228.
[50] Y. Liu et al., *ACS Nano* **2018**, 12, 7174.
[51] Y. Liu et al., *Nano Lett* **2018**, 18, 2557.
[52] P. A. Lee, N. Nagaosa, X.-G. Wen, *Rev Mod Phys* **2006**, 78, 17.
[53] A. F. Ioffe, *Academic Press*, New York, **1960**.
[54] R. Takahashi, N. Terakado, Y. Yamazaki, Y. Takahashi, T. Fujiwara, *J Ceram Soc Jpn* **2017**, 125, 423.
[55] J. Y. Song, B. C. Zhao, Y. N. Huang, Y. F. Qin, J. F. Zhou, W. H. Song, Y. P. Sun, *J Alloys Compd* **2017**, 695, 2506.
[56] J.-H. Choi, T. C. Messina, J. Yan, G. I. Drandova, J. T. Markert, *J Magn Magn Mater* **2004**, 272–276, 970.
[57] C. G. S. Pillai, A. M. George, *Int J Thermophys* **1986**, 7, 1091.
[58] J. E. Rodríguez, J. López, Physica B Condens Matter **2007**, 387, 143.
[59] P. Prayoonphokkharat, P. Amonpattaratkit, A. Kosuga, A. Watcharapasorn, *J Alloys Compd* **2021** 871, 159552.
[60] S. Li, S. Guo, Y. Xu, J. Zhou, X. Chen, *ACS Appl Electron Mater* **2022**, 4, 787.
[61] A. Miura, T. Kikkawa, R. Iguchi, K. Uchida, E. Saitoh, J. Shiomi, *Phys Rev Mater* **2017**, 1, 014601.
[62] X. W. Zhu, Y. Sakka, Y. Zhou, K. Hirao, K. Itatani, *J Eur Ceram Soc* **2014**, 34, 2585.
[63] S. Honda, S. Hashimoto, S. Iwata, Y. Iwamoto, *Ceram Int* **2016**, 42, 1453.
[64] Y. Shen, D. R. Clarke, P. A. Fuierer, *Appl Phys Lett* **2008**, 93, 102907.
[65] R. S. C. Bose, V. Sheoran, P. S. H. Vaishnavi, D. S. Prem, S. Chakravarty, R. Raman, D. A. Babu, P. Saharan, S. Nair, J. Ram, *J Alloys Compd* **2021**, 859, 157828.
[66] S. R. Popuri, M. Pollet, R. Decourt, F. D. Morrison, N. S. Bennett, J. W. G. Bos, *J Mater Chem C Mater* **2016**, 4, 1685.
[67] D. Kenfaui, B. Lenoir, D. Chateigner, B. Ouladdiaf, M. Gomina, J. G. Noudem, *J Eur Ceram Soc* **2012**, 32, 2405.
[68] J. X. Xue, J. X. Liu, B. H. Xie, G. J. Zhang, *Scr Mater* **2011**, 65, 966.
[69] F. L. Levy, *Int. J. Refrig* **1981**, 4, 223.
[70] D. S. Smith, A. Alzina, J. Bourret, B. Nait-Ali, F. Pennec, N. Tessier-Doyen, K. Otsu, H. Matsubara, P. Elser, U. T. Gonzenbach, *J Mater Res* **2013**, 28, 2260.
[71] A. V. Sologubenko, T. Lorenz, H. R. Ott, A. Freimuth, *J Low Temp Phys* **2007**, 147, 387.
[72] C. Hess, *Eur Phys J Spec Top* **2007**, 151, 73.
[73] A. L. Chernyshev, A. V. Rozhkov, *Phys Rev B* **2005**, 72, 104423.
[74] D. Msika et al., *Phys Rev B* **2023**, 107, 104420.
[75] A. P. Ramirez, S. W. Cheong, M. L. Kaplan, *Phys Rev Lett* **1994**, 72, 3108.
[76] K. Karmakar, R. Bag, M. Skoulatos, C. Rüegg, S. Singh, *Phys Rev B* **2017**, 95, 235154.
[77] J. G. Cheng, J. S. Zhou, J. B. Goodenough, Y. T. Su, Y. Sui, Y. Ren, *Phys Rev B* **2011**, 84, 104415.
[78] M. Matsukawa, T. Mizukoshi, K. Noto, Y. Shiohara, *Phys Rev B* **1996**, 53, R6034.
[79] D. T. Morelli, J. Heremans, G. Doll, P. J. Picone, H. P. Jenssen, M. S. Dresselhaus, *Phys Rev*

B **1989**, 39, 804.

[80] J. Callaway, R. Boyd, *Physical Review* **1964**, 134, A1655.

[81] X. F. Sun, J. Takeya, S. Komiya, Y. Ando, *Phys Rev B* **2003**, 67, 104503.

[82] C. Hess, C. Baumann, U. Ammerahl, B. Büchner, F. Heidrich-Meisner, W. Brenig, A. Revcolevschi, *Phys Rev B* **2001**, 64, 184305.